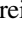






# Discovery of X-Rays from the Old and Faint Pulsar J1154–6250

Andrei P. Igoshev<sup>1</sup> , Sergey S. Tsygankov<sup>2,3</sup> , Michela Rigoselli<sup>4,5</sup>, Sandro Mereghetti<sup>4</sup> , Sergei B. Popov<sup>6</sup>, Justin G. Elfritz<sup>7</sup>, and Alexander A. Mushtukov<sup>3,7,8</sup>

<sup>1</sup> Department of Physics, Technion Israel Institute of Technology, Haifa 3200003, Israel; [ignotur@gmail.com](mailto:ignotur@gmail.com), [ignotur@physics.technion.ac.il](mailto:ignotur@physics.technion.ac.il)

<sup>2</sup> Department of Physics and Astronomy, FI-20014 University of Turku, Finland

<sup>3</sup> Space Research Institute of the Russian Academy of Sciences, Profsoyuznaya Str. 84/32, Moscow 117997, Russia

<sup>4</sup> INAF, Istituto di Astrofisica Spaziale e Fisica Cosmica Milano, via E. Bassini 15, I-20133 Milano, Italy

<sup>5</sup> Dipartimento di Fisica G. Occhialini, Università degli Studi di Milano Bicocca, Piazza della Scienza 3, I-20126 Milano, Italy

<sup>6</sup> Sternberg Astronomical Institute, Lomonosov Moscow State University, Universitetsky prospekt 13, 119234, Moscow, Russia

<sup>7</sup> Anton Pannekoek Institute, University of Amsterdam, Science Park 904, 1098 XH Amsterdam, The Netherlands

<sup>8</sup> Pulkovo Observatory, Russian Academy of Sciences, Saint Petersburg 196140, Russia

Received 2018 June 1; revised 2018 August 27; accepted 2018 August 27; published 2018 September 28

## Abstract

We report on the first X-ray observation of the 0.28 s isolated radio pulsar PSR J1154–6250 obtained with the *XMM-Newton* observatory in 2018 February. A point-like source is firmly detected at a position consistent with that of PSR J1154–6250. The two closest stars are outside the  $3\sigma$  confidence limits of the source position and thus unlikely to be responsible for the observed X-ray emission. The energy spectrum of the source can be fitted equally well either with an absorbed power law with a steep photon index  $\Gamma \approx 3.3$  or with an absorbed blackbody with temperature  $kT = 0.21 \pm 0.04$  keV and emitting radius  $R_{\text{BB}} \approx 80$  m (assuming a distance of 1.36 kpc). The X-ray luminosity of  $4.4 \times 10^{30}$  erg s<sup>-1</sup> derived with the power-law fit corresponds to an efficiency of  $\eta_X = L_X^{\text{unabs}}/\dot{E} = 4.5 \times 10^{-3}$ , similar to those of other old pulsars. The X-ray properties of PSR J1154–6250 are consistent with an old age and suggest that the spatial coincidence of this pulsar with the OB association Cru OB1 is due to a chance alignment.

*Key words:* methods: observational – pulsars: individual (J1154–6250) – stars: neutron – X-rays: stars

## 1. Introduction

Rotation-powered pulsars were first discovered as radio sources emitting pulses at extremely precise periodic intervals (Hewish et al. 1968), and later detected also in the optical (Cocke et al. 1969), X-ray (Halpern & Holt 1992; Oegelman et al. 1993), and  $\gamma$ -ray bands. Their properties are well explained by a model of an isolated rotating neutron star (NS) with magnetic field  $B \sim 10^{12}$  G (Gold 1969; Ruderman & Sutherland 1975). From the rotation period  $P$  and its time derivative  $\dot{P}$ , one can define a characteristic age  $\tau = P/(2\dot{P})$  and measure the rotational energy loss rate  $\dot{E} = -4\pi^2 I \dot{P}/P^3$ , where  $I$  is the NS moment of inertia.

The X-ray properties of isolated radio pulsars (see Harding 2013 for a review) depend on their age. The youngest,  $\tau < 10^4$  yr, and most energetic,  $\dot{E} > 10^{36}$  erg s<sup>-1</sup>, objects emit mainly non-thermal radiation, with strong pulsations and a spectrum well described by a power-law model. At intermediate stages,  $10^4 < \tau < 10^6$  yr, when the NS is still hot, pulsars show a combination of magnetospheric non-thermal and thermal emission from the whole surface, the latter typically described, as a first approximation, by a blackbody model. Without additional heating mechanisms, unlike the magnetar case, an NS typically reaches a thermal luminosity of  $\sim 10^{30}$  erg s<sup>-1</sup> in  $\lesssim 1$  Myr (Page et al. 2004). At characteristic ages larger than  $\approx 1$  Myr, the NS cools down in the absence of heating sources (Yakovlev & Pethick 2004) and its surface radiation becomes undetectable for currently available X-ray telescopes.

However, some of these old objects show thermal emission with temperature  $kT \approx 0.1$ – $0.3$  keV and emission radius  $R_{\text{BB}} \approx 10$ – $200$  m (see, e.g., Zavlin & Pavlov 2004; Gil et al. 2008; Misanovic et al. 2008; Kargaltsev et al. 2012; Mereghetti et al. 2016; Hermsen et al. 2017; Rigoselli & Mereghetti 2018).

The thermal emission in these old pulsars is interpreted as radiation from a polar cap heated by particles accelerated in the magnetosphere (Harding & Muslimov 2001, 2002). The size of the cap, as estimated from blackbody fits to the X-ray spectra, is often smaller than that predicted by theory in the case of a dipolar field, but fitting the spectra with NS atmosphere (NSA) models (Zavlin & Pavlov 2004) yields in some cases emission regions with a size consistent with the predicted values. If old pulsars show only non-thermal emission, the X-ray efficiency (the ratio of the X-ray luminosity to the spin-down energy loss rate) often exceeds the values seen in younger pulsars (Kargaltsev et al. 2006). The reason for this is unknown, but it could be partly explained by a selection effect. So, a larger sample and longer exposures are needed to gain a better understanding of the X-ray emission of old radio pulsars (Posselt et al. 2012b).

It must also be considered that the spin-down age  $\tau$ , which is used to interpret the X-ray properties, is a reasonable estimate of the true age of a pulsar only if two conditions are met: (1) the initial rotational period is much smaller than its current value and (2) the braking index  $n = 2 - P\ddot{P}/\dot{P}^2 \equiv 3$ . From observations it is known that, in some cases, the initial period can be quite long and comparable with the observed period (Popov & Turolla 2012). The observed braking indices range from 0.9(2) for PSR J1734–3333 to 3.15(3) for PSR J1640–4631 (Espinoza et al. 2011; Archibald et al. 2016). The difference with respect to the expected value  $n = 3$  could be caused by deviation from counter-alignment between the rotational axis and the orientation of the magnetic dipole (Philippov et al. 2014) or by some evolution of the magnetic field.

**Table 1**  
Observed and Derived Parameters for PSR J1154–6250

Parameter	Value
R.A. (J2000.0)	11 <sup>h</sup> 54 <sup>m</sup> 20 <sup>s</sup> .1(1)
Decl. (J2000.0)	−62°50′02″.7(7)
Period $P$ (s)	0.28201171065(3)
Period derivative $\dot{P}$ (s s <sup>−1</sup> )	$5.59(5) \times 10^{-16}$
Spin-down age $\tau$ (yr)	$8 \times 10^6$
Surface dipolar magnetic field $B$ (G)	$4.0 \times 10^{11}$
Spin-down energy loss rate $\dot{E}$ (erg s <sup>−1</sup> )	$9.8 \times 10^{32}$
Dispersion measure DM (cm <sup>−3</sup> pc)	74(6)
Distance based on DM (kpc)	1.36 <sup>a</sup>

**Notes.** Information is based on Kramer et al. (2003) and the ATNF pulsar catalog. Numbers in parentheses show the uncertainty for the last digits.

<sup>a</sup> Distance is derived using the electron density model of Yao et al. (2017).

Here we report on a recent X-ray observation of the rotation-powered pulsar PSR J1154–6250 obtained with the *XMM-Newton* satellite. The main parameters of PSR J1154–6250 are summarized in Table 1, based on the information in the ATNF pulsar catalog v.1.58<sup>9</sup> (Manchester et al. 2005). The dispersion measure corresponds to a distance of 1.77 kpc according to the NE2001 electron density model (Cordes & Lazio 2002) and to 1.36 kpc according to the newer model by Yao et al. (2017). In the following we use  $d = 1.36$  kpc.

PSR J1154–6250 is located at an angular distance of 1.6 degrees from the center of the OB association Cru OB1 (Mel’Nik & Dambis 2009), which has coordinates R.A. = 11<sup>h</sup>40<sup>m</sup>00<sup>s</sup>.0 decl. = −62°54′00″. A typical size of the association of 40 pc translates to 1°9′ at 2 kpc distance. Thus PSR J1154–6250 could be associated with Cru OB1, implying a true age much smaller than its characteristic age. NSs are known to receive large natal kicks at the moment of their formation (Lyne & Lorimer 1994; Verbunt et al. 2017), with average speed 370 km s<sup>−1</sup> which translates to a traveled distance  $\approx 3$  kpc in 8 Myr. The natal kick makes these objects oscillate in the Galactic potential. The time interval of  $\tau < 20$  Myr is not enough to finish half of the oscillation in the potential, so NSs with ages in the range 1–20 Myr could be projected onto the OB association only if they move along the Galactic disc, which is a rare situation. Among NSs with such spin-down ages there could be objects with complicated magnetic field evolution, caused for example by the fall-back of matter after the supernova explosion (Chevalier 1989) and subsequent magnetic field re-emergence (Ho 2011; Viganò & Pons 2012; Igoshev et al. 2016). So the primary goal of this research is to check if PSR J1154–6250 is as old as apparent from its spin-down age.

## 2. Observations and Data Reductions

The observations were performed on 2018 February 8 with the *XMM-Newton* telescope, using the European Photon Imaging Camera (EPIC). All the EPIC cameras, the pn and the two MOS (Strüder et al. 2001; Turner et al. 2001), were used in full-frame mode and with a thin optical filter (see Table 2). The nominal exposure was 60 ks. The analysis was done using the *XMM-Newton* Science Analysis System (SAS) package version 16.1.0.

<sup>9</sup> <http://www.atnf.csiro.au/research/pulsar/psrcat/>

Since the object is quite dim, we performed the analysis with two different methods adequate for faint sources: (1) a traditional spectral analysis, based on source and background extraction regions, but using the  $W$ -statistics for the spectral fits (Wachter et al. 1979), and (2) a maximum likelihood (ML) method (Hermsen et al. 2017; Rigoselli & Mereghetti 2018).

### 2.1. Traditional Analysis

Using the source detection pipeline of the SAS, we detected with a likelihood of 36 a point source with  $81 \pm 15$  pn counts (0.2–12 keV energy range) close to the pulsar position. We improved the *XMM-Newton* astrometry using the second *Gaia* data release, as described in the Appendix. The corrected source coordinates were R.A. = 11<sup>h</sup>54<sup>m</sup>20<sup>s</sup>.52 and decl. = −62°50′03″.6 (J2000.0), with an error of 1″.2. This position differs by 3″ (corresponding to  $2.5\sigma$ ) from that of PSR J1154–6250, determined by means of timing radio observations (see Table 1 and Figure 1). We note that the closest stars to the X-ray positions are at more than 4″, i.e., outside the  $3\sigma$  error radius. We consider it unlikely that one of them could be the counterpart of the detected X-ray source, which we therefore identify with PSR J1154–6250.

Due to the limited flux from the source, we analyzed events recorded by the three cameras of the EPIC instrument: both MOS and pn. We created good time intervals (GTIs) excluding background flare periods (count rates exceeding 2.46, 3.43, and 9.5 counts s<sup>−1</sup> for MOS1, MOS2, and pn, respectively) identified by the procedure of signal-to-noise ratio optimization described in Rosen et al. (2016). After GTI filtering, we kept only the events in the range 0.2–10 keV that satisfy standard pattern requirements ( $PATTERN \leq 12$  for MOS and  $PATTERN \leq 4$  for pn) and quality flags.

The source spectrum was extracted from a circle centered at the radio coordinates and with radius 15 arcsec. The background spectrum was extracted from a circle centered at R.A. = 11<sup>h</sup>54<sup>m</sup>30<sup>s</sup>.6 and decl. = −62°50′14″.8 with radius 32 arcsec. The auxiliary and response files for the spectral analysis were prepared using the standard tasks `rmfgen` and `arfgen`. We combined the MOS1 and MOS2 spectra into a single file using `epicspeccombine` and analyzed them using an averaged response matrix.

We fitted simultaneously the pn and MOS spectra using version 12.9.1 of the `xspec` software. For the interstellar absorption we adopted the `tbabs` model which is based on photoionization cross-sections by Wilms et al. (2000).

Due to the small count rate we rebinned the spectra to have one count per energy bin and used  $W$ -statistics (`cstat` option in `xspec`; Wachter et al. 1979), which is a version of  $C$ -statistics (Cash 1979) applied if no model for the background radiation is provided. A comparison of different models was done by means of the Akaike information criterion (AIC, see Akaike 1974), which is used in astronomy (Liddle 2007) and in particular in X-ray astronomy to discriminate between different spectral models (Tsygankov et al. 2017). The value of AIC is computed as  $AIC = 2k + C$ , where  $C$  is the minimum value of statistics and  $k$  the number of model parameters. A difference of 10 between the AIC values computed for two models is significant to choose the best model and corresponds to a case when one model is  $\exp(10/2) \approx 150$  times more probable than the other.

**Table 2**  
Details of the *XMM-Newton* Observation

Pulsar	Obs. ID	Start Time UT	End Time UT	Effective Exposure (s)		
				pn	MOS1	MOS2
PSR J1154–6250	0804240201	2018 Feb 08 01:11:59	2018 Feb 08 18:10:02	49950	58900	58900

## 2.2. Maximum Likelihood Analysis

The ML method estimates the most probable number of source and background counts by comparing the spatial distribution of the observed counts with the expected distribution of a model in which there is a source and a uniform background. The expected spatial distribution of the counts for a point source is given by the instrument point-spread function (PSF). We used the MOS and pn PSF derived from the *XMM-Newton* in-flight calibrations,<sup>10</sup> with parameters appropriate for the average energy value in each of the considered bins.

We used single- and multiple-pixel events for both the pn and MOS. The events detected in the two MOS cameras were combined into a single data set, and we used averaged response files.

Since with the ML analysis it is possible to derive an accurate estimate of the background at the source position, it was not necessary to remove time intervals of high background. We applied the ML in a circular region positioned to avoid the gaps between the CCD chips (radius of 60", center at R.A. = 11<sup>h</sup>54<sup>m</sup>23<sup>s</sup>.2, decl. = –62°49'47"). For the spectral extraction we fixed the source position at the coordinates found by the ML in the pn+MOS image in the 0.4–2 keV range (R.A. = 11<sup>h</sup>54<sup>m</sup>20<sup>s</sup>.4, decl. = –62°50'04".4). This position is consistent with that found with the SAS pipeline.

In the energy range 0.4–2 keV the source was detected with  $113 \pm 21$  counts (pn) and  $66 \pm 15$  counts (MOS), which correspond to a total count rate of  $(3.4 \pm 0.5) \times 10^{-3}$  count s<sup>-1</sup>.

The energy bins for the spectral analysis were chosen from the requirement to have a signal-to-noise ratio greater than 2.5 $\sigma$  in each spectral channel. This resulted in four energy bins for the pn and three for the MOS. Below 0.4 keV and above 2 keV, the source detection was below our significance threshold; therefore we derived upper limits on the source counts in these energy bins.

## 3. Possible Optical Counterparts

In the *Gaia* database there are no stars closer than 4" to the corrected X-ray position; see Figure 1. The closest object, at 4"06, is *Gaia* DR 2 5334588220496359424 which has  $g = 17.48$ . A slightly brighter star, *Gaia* DR2 5334588151811060992 with  $g = 14.15$ , is located at 4"29. It has  $B = 16.4$ ,  $I = 13.11$ ,  $J = 11.937$ , and  $K = 10.951$ , while the fainter source has  $B = 19.6$ ,  $I = 16.08$ ,  $J = 14.07$ , and  $K = 12.86$  (Epchtein et al. 1999). Based on the color differences  $I - J$  and  $J - K$ , we identify the brighter star as a main sequence star of spectral type K5 and the fainter one as an M5 star.

We fitted the spectra of our X-ray source with thermal plasma models (apec by Smith et al. 2001; mekal by Mewe et al. 1985), as expected in the case of coronal emission from normal stars. Acceptable fits could be obtained with temperatures in the range  $kT = 0.23$ – $0.26$  keV, absorption

$N_H \sim 10^{22}$  cm<sup>-2</sup>, and flux  $\sim 3 \times 10^{-15}$  erg cm<sup>-2</sup> s<sup>-1</sup>. The resulting X-ray-to-optical flux ratios  $\log(f_x/f_j) = \log(f_x) + 0.4J + 6.30$  (Agüeros et al. 2009) were –3.34 and –2.6 for the K and M star, respectively. These values are compatible with X-ray emission from late-type stars and therefore we cannot exclude these objects as potential counterparts of the X-ray source based on spectral and/or flux arguments. However, we note that both stars are outside the 3 $\sigma$  confidence level error circle of the X-ray source and therefore we consider that PSR J1154–6250 is much more likely responsible for the detected X-ray emission.

## 4. Results

The results of the spectral analysis obtained with the two methods are summarized in Table 3. The absorption column density was poorly constrained due to the small count rate, so we decided to fix it at  $N_H = 2.2 \times 10^{21}$  cm<sup>-2</sup>, which follows from the relation between dispersion measure and  $N_H$  for radio pulsars (He et al. 2013).

With the traditional analysis the absorbed blackbody model fits the data slightly better; however the difference of 3.68 in the AIC values is not enough to prefer this model to the power law. The ML analysis provides results in full agreement with those of the traditional analysis. Also in this case, both the blackbody and power-law models are acceptable (see Figure 2).

With a power-law model we find a rather high photon index value,  $\Gamma \approx 3.3$ , but still compatible with the range of  $\Gamma = 2$ – $4$  noted by Posselt et al. (2012b). The unabsorbed flux is  $F_{0.2-10 \text{ keV}}^{\text{unabs}} = (2.6_{-1.0}^{+1.6}) \times 10^{-14}$  erg s<sup>-1</sup> cm<sup>-2</sup>.

For the blackbody model we obtain a temperature  $kT = 0.21 \pm 0.04$  keV and a radius of the emitting region  $R_{\text{BB}} = 81_{-29}^{+46}$  m, which corresponds to a bolometric luminosity  $L_{\text{bol}} = \pi R_{\text{BB}}^2 \sigma_B T^4 = 4 \times 10^{29}$  erg s<sup>-1</sup>, where  $\sigma_B$  is the Stefan–Boltzmann constant. The radius and temperature anticorrelate with each other, as shown in Figure 3. The unabsorbed flux is  $7.5_{-2.0}^{+2.2} \times 10^{-15}$  erg s<sup>-1</sup> cm<sup>-2</sup>. The values of  $kT$  and  $R_{\text{BB}}$  found in our fit are similar to those found for old radio pulsars with thermal emission (see, e.g., Misanovic et al. 2008; Mereghetti et al. 2016).

We also tried fits with the NSA model for thermal emission from an NS hydrogen atmosphere (Zavlin et al. 1996) with fixed parameters NS mass  $M_{\text{NS}} = 1.4 M_{\odot}$  and radius  $R_{\text{NS}} = 10$  km and  $N_H = 2.2 \times 10^{21}$  cm<sup>-2</sup>. This model gave  $\log T_{\text{eff}} [\text{K}] = 6.15 \pm 0.15$ ,  $R_{\text{BB}} = 350$  m, with  $C$ -value/d.o.f. = 197.02/212. The NSA model might not be the best choice since the magnetic field of PSR J1154–6250 is  $4 \times 10^{11}$  G, which is not covered by this model.

## 5. Discussion

### 5.1. Size of the Polar Cap and Multipoles

The X-ray emission from PSR J1154–6250 has typical properties of old radio pulsars, in particular a small thermal luminosity of  $\sim 4 \times 10^{29}$  erg s<sup>-1</sup>. We can also safely assume

<sup>10</sup> <https://www.cosmos.esa.int/web/xmm-newton/calibration-documentation>



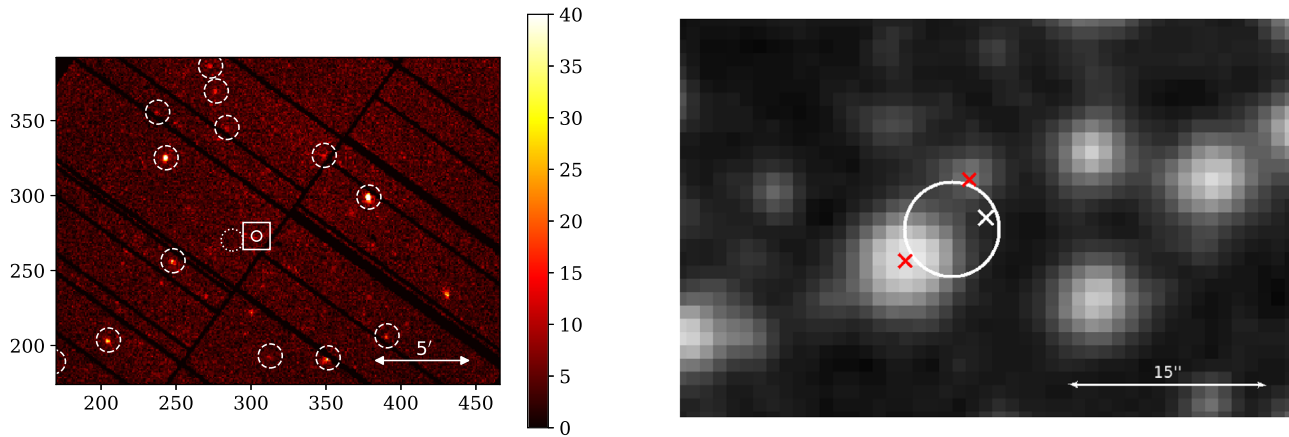


**Figure 1.** Filtered EPIC pn image (energy range 0.3–2 keV) of the field binned into four pixels per bin (left panel). The white rectangle region is scaled and shown in the right panel based on the DSS2 survey (emulsion and filter IIIaF+OG590; bandpass peaks at around 6500 Å, which corresponds to red). White solid circles show the spectral extraction region used in the traditional approach (left panel) and  $3\sigma$  confidence interval for coordinates of the X-ray source (right panel). White dashed circles are locations of sources used to improve astrometry in the field. The white dotted circle shows the location of the background extraction region used in the traditional approach. Red crosses show exact positions of the closest stars in the second *Gaia* data release. The white cross is the radio position of the PSR J1154–6250. The color bar shows the number of counts per bin.

that the hot spot is not formed due to the presence of a strong toroidal crust-confined magnetic field since its size is well below  $10^\circ$ – $40^\circ$  of latitude of the NS surface (Aguilera et al. 2008), which would correspond to a spot size of 1.7–7 km. The only plausible mechanism leading to the formation of such tiny spots is surface heating by accelerated particles moving along the open field lines.

The size of the polar cap heated by the infalling accelerated particles depends strongly on the configuration of the magnetic field. The polar cap radius in the case of a pure dipole magnetic field is

$$R_{\text{PC}} = \sqrt{\frac{2\pi R_{\text{NS}}^3}{cP}} \quad (1)$$

where  $c$  is the speed of light. For PSR J1154–6250 this gives  $R_{\text{PC}} \approx 270$  m (for an assumed  $R_{\text{NS}} = 10$  km), which is much larger than the value of the emitting radius derived from our blackbody fit. It is worth mentioning that the fit of the spectra using the NS hydrogen atmosphere model gives an estimate of  $R_{\text{BB}}$  compatible with  $R_{\text{PC}}$ . The discrepancy between  $R_{\text{BB}}$  and  $R_{\text{PC}}$  in the case of the absorbed blackbody model could indicate the presence of high-order magnetic multipoles. These can increase the curvature of the magnetic field lines, resulting in a reduction of the polar cap size. This is not surprising since PSR J1154–6250 lies below the death line derived for a pure dipolar magnetic field (Ruderman & Sutherland 1975; Chen & Ruderman 1993; Zhang et al. 2000):

$$\log \dot{P} = \frac{11}{4} \log P - 14.62, \quad (2)$$

which results in  $\log \dot{P} = -16.13$  for  $P = 0.28$  s, while the pulsar has  $\log \dot{P} = -16.74$ . The small-scale magnetic field structure could explain both the small size of the polar cap and the presence of radio emission. Another possibility is that the small apparent size of the blackbody emitting region is simply due to a geometric projection effect.

Of course, if the pulsar distance were a factor  $\sim 4$  larger than assumed here, the polar cap size would correspond to the dipolar one. Such a distance is allowed by the large

uncertainties of the electron density model in rare cases (Arzoumanian et al. 2018). On the other hand, the older electron density model NE2001 (Cordes & Lazio 2002) provides a distance only 1.3 times larger. The unknown equation of state for the NS matter could hardly ever contribute to this uncertainty since a range of 10.0 km up to 11.5 km (Özel & Freire 2016) results only in  $\approx 20\%$  variation in the polar cap radius.

## 5.2. Comparison with Other Pulsars

It is known that old radio pulsars tend to have a higher efficiency of X-ray emission compared to young pulsars (Posselt et al. 2012b). The X-ray efficiency  $\eta_X$  is the ratio of X-ray luminosity  $L_X^{\text{nontherm}}$  to  $\dot{E}$ :

$$\eta_X = \frac{4\pi D^2 F_{0.2-10 \text{ keV}}^{\text{unabs}}}{\dot{E}} \approx 4.5 \times 10^{-3} \quad (3)$$

under the assumption of isotropic emission and using the flux obtained with the traditional analysis. If we interpret the X-ray emission of PSR J1154–6250 as non-thermal, we see that its efficiency is very similar to that of other old pulsars, e.g., comparable with that of PSR J0108–1431 (Posselt et al. 2012a) and 2–3 orders of magnitude higher than that of young radio pulsars; see, e.g., Figure 5 in Posselt et al. (2012b). In particular this efficiency is higher than  $2 \times 10^{-3}$ , which is expected from the relation by Possenti et al. (2002). It is worth noting that the relation of Possenti et al. was derived for X-ray luminosities in the 2–10 keV energy band where we see virtually no emission from our object.

The power-law exponent found in our analysis is  $\Gamma \approx 3.3$ . This value is well within range described by Posselt et al. (2012b). The value  $\Gamma = 3.1$  was found for another old pulsar, PSR J2043+2740 ( $\tau = 1.2$  Myr), by Becker et al. (2004).

## 6. Conclusions

We have detected for the first time the X-ray emission from the old radio pulsar PSR J1154–6250 using the *XMM-Newton* observatory. The faintness of the source does not allow us

**Table 3**  
Results of the Spectral Analysis

Model	$N_{\text{H}}$ $10^{22} \text{ cm}^{-2}$	$\Gamma$	Norm. <sup>a</sup>	$kT$ keV	$R_{\text{BB}}^{\text{b}}$ m	$F_{0.2-10 \text{ keV}}^{\text{abs}}$ $10^{-15} \text{ erg s}^{-1} \text{ cm}^{-2}$	$F_{0.2-10 \text{ keV}}^{\text{unabs}}$ $10^{-15} \text{ erg s}^{-1} \text{ cm}^{-2}$	Statistics
Traditional Analysis								
PL	0.22	$3.1_{-0.4}^{+0.5}$	$2.4 \pm 0.6$	...	...	$4.3 \pm 1.1$	$20 \pm 5$	201.56/212
BB	0.22	...	...	$0.22_{-0.04}^{+0.05}$	$73_{-30}^{+49}$	$3.1 \pm 0.7$	$7.4 \pm 1.8$	197.88/212
Maximum Likelihood Analysis								
PL	0.22	$3.6_{-0.4}^{+0.5}$	$2.0 \pm 0.5$	...	...	$3.1 \pm 0.9$	$26_{-10}^{+16}$	1.40/9
BB	0.22	...	...	$0.21_{-0.03}^{+0.04}$	$81_{-29}^{+46}$	$2.9 \pm 0.7$	$7.5_{-2.0}^{+2.2}$	0.40/9

**Notes.** The best-fit values and 90% confidence limits.

<sup>a</sup>  $10^{-6}$  photons  $\text{cm}^{-2} \text{ s}^{-1} \text{ keV}^{-1}$  at 1 keV.

<sup>b</sup> Blackbody radius for an assumed distance of 1.36 kpc.

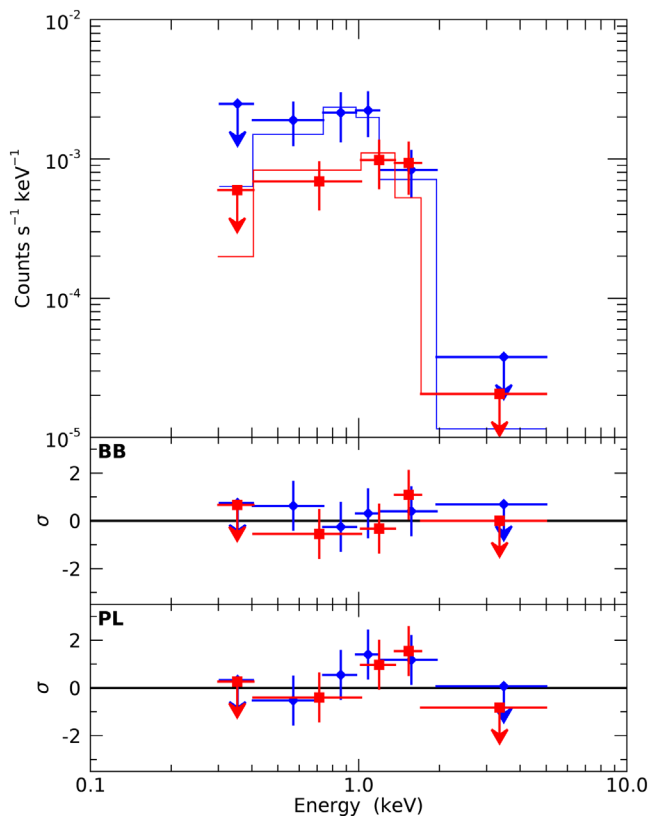


**Figure 2.** EPIC pn (blue diamonds) and MOS (red squares) X-ray spectra of PSR J1154–6250 extracted with the maximum likelihood method. The best-fit blackbody model is shown in the top panel, and the corresponding residuals in the middle panel. The bottom panel shows the residuals obtained by fitting the spectra with a power law.

to clearly discriminate between emission of thermal or non-thermal origin.

In any case the spectrum is rather soft: a power law with photon index  $\Gamma \approx 3.3$  or a blackbody with temperature  $kT = 0.21$  keV. If the emission is non-thermal, the implied X-ray efficiency is similar to that of other pulsars of similar age. If, instead, it is of thermal origin, the low flux implies emission from a small region of radius  $\approx 80$  m, most likely a polar cap reheated by back-flowing magnetospheric particles.

All these properties of PSR J1154–6250 are similar to those of other old radio pulsars. Therefore, we conclude that PSR

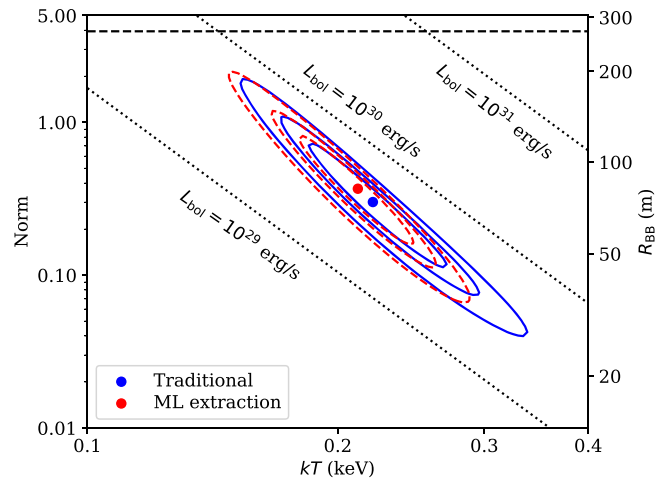


**Figure 3.** Most probable value (dot) and confidence intervals (1, 2, and  $3\sigma$ ) of temperature and emission radius for the blackbody model. Traditional analysis is represented by the solid blue lines, while the maximum likelihood technique is shown by the dashed red lines. The dashed horizontal line shows the size of the dipolar polar cap calculated using Equation (1) and assuming an NS radius of 10 km. The normalization is computed as  $R_{\text{km}}^2/D_{10}^2$  where  $R_{\text{km}}$  is the emission radius in km and  $D_{10}$  is the distance to the source in units of 10 kpc.

J1154–6250 is old and its projection on the OB association Cru OB1 is most likely a chance coincidence.

A.I. would like to acknowledge support from the Israel science foundation (ISF) I–CORE grant 1829/12. The work of S.P. was supported by the RSF grant 14-12-00146. This research was also supported by the grant 14.W03.31.0021 of the Ministry of Education and Science of the Russian Federation (S.T. and A.M.). J.E. acknowledges partial support from NWO VIDI award A.2320.0076. We thank an anonymous referee for comments which helped to improve the manuscript.

This work is based on observations obtained with XMM-Newton, an European Space Agency (ESA) science mission with instruments and contributions directly funded by ESA Member States and NASA. We used data from the ESA mission *Gaia* (<https://www.cosmos.esa.int/gaia>), processed by the *Gaia* Data Processing and Analysis Consortium (DPAC, <https://www.cosmos.esa.int/web/gaia/dpac/consortium>). Funding for the DPAC has been provided by national institutions, in particular the institutions participating in the *Gaia* Multilateral Agreement.

This research made use of the cross-match service provided by CDS, Strasbourg.

The Digitized Sky Surveys were produced at the Space Telescope Science Institute under U.S. Government grant NAG W-2166. The images of these surveys are based on photographic data obtained using the Oschin Schmidt Telescope on Palomar Mountain and the UK Schmidt Telescope. The plates were processed into the present compressed digital form with the permission of these institutions.

*Facility:* XMM-Newton.

*Software:* astropy (Astropy Collaboration et al. 2013), SAS (v16.1.0 Gabriel et al. 2004), XSPEC (v12.9.1 Arnaud 1996).

## Appendix Improving the Astrometry for the X-Ray Source

To improve the accuracy on the position of the detected X-ray source we corrected the XMM-Newton astrometry using the second Gaia data release (Gaia Collaboration et al. 2016, 2018). We first selected 26 point-like X-ray sources detected in the pn image with the highest significance by means of the `edetect_chain` (excluding the source under study). This list of X-ray sources was then cross-matched with the second Gaia data release based on coordinates coincident within a circle of  $4''$ . From the resulting list we then selected only those objects with a ratio of X-ray to optical flux  $\log f_x/f_G < -0.5$ . Objects with  $\log f_x/f_G > -0.5$  are expected to be galaxies for which the second Gaia data release does not provide precise positions. Since the Gaia G band is quite similar to the V band of the Johnson system, especially if  $(B-V) \approx 0$  (Jordi et al. 2010), we computed  $f_x/f_G$  as  $\log f_x/f_G = \log f_x + 0.4g + 5.37$ . We optimized the residuals between the X-ray pn and the Gaia coordinates, allowing rotation and translation of the X-ray frame using `astropy` (Astropy Collaboration et al. 2013). After a first optimization, we removed sources with residual distances larger than  $3''$  and optimized again. This optimization procedure for 17 sources decreased the mean displacement from the initial value of  $1''.33$  to  $\sigma_{\text{fit}} = 1''.21$ . From the fit we concluded that the relative astrometric uncertainty is  $3\sigma_{\text{fit}} = 3''.63$ . Since the Gaia astrometric accuracy for stars with  $g < 18^m$  is  $< 0.07$  mas, the main source of uncertainty is the statistical error on the X-ray positions.

## ORCID iDs

Andrei P. Igoshev  <https://orcid.org/0000-0003-2145-1022>

Sergey S. Tsygankov  <https://orcid.org/0000-0002-9679-0793>

Sandro Mereghetti  <https://orcid.org/0000-0003-3259-7801>

## References

Agüeros, M. A., Anderson, S. F., Covey, K. R., et al. 2009, *ApJS*, **181**, 444  
 Aguilera, D. N., Pons, J. A., & Miralles, J. A. 2008, *A&A*, **486**, 255  
 Akaike, H. 1974, *ITAC*, **19**, 716  
 Archibald, R. F., Gotthelf, E. V., Ferdman, R. D., et al. 2016, *ApJL*, **819**, L16  
 Arnaud, K. A. 1996, in ASP Conf. Ser. 101, *Astronomical Data Analysis Software and Systems V*, ed. G. H. Jacoby & J. Barnes (San Francisco, CA: ASP), 17

Arzoumanian, Z., Brazier, A., Burke-Spolaor, S., et al. 2018, *ApJS*, **235**, 37  
 Astropy Collaboration, Robitaille, T. P., Tollerud, E. J., et al. 2013, *A&A*, **558**, A33  
 Becker, W., Weisskopf, M. C., Tennant, A. F., et al. 2004, *ApJ*, **615**, 908  
 Cash, W. 1979, *ApJ*, **228**, 939  
 Chen, K., & Ruderman, M. 1993, *ApJ*, **402**, 264  
 Chevalier, R. A. 1989, *ApJ*, **346**, 847  
 Cocke, W. J., Disney, M. J., & Taylor, D. J. 1969, *Natur*, **221**, 525  
 Cordes, J. M., & Lazio, T. J. W. 2002, arXiv:astro-ph/0207156  
 Epchtein, N., Deul, E., Derriere, S., et al. 1999, *A&A*, **349**, 236  
 Espinoza, C. M., Lyne, A. G., Kramer, M., Manchester, R. N., & Kaspi, V. M. 2011, *ApJL*, **741**, L13  
 Gabriel, C., Denby, M., Fyfe, D. J., et al. 2004, in ASP Conf. Ser. 314, *Astronomical Data Analysis Software and Systems (ADASS) XIII*, ed. F. Ochsenbein, M. G. Allen, & D. Egret (San Francisco, CA: ASP), 759  
 Gaia Collaboration, Brown, A. G. A., Vallenari, A., et al. 2018, arXiv:1804.09365  
 Gaia Collaboration, Prusti, T., de Bruijne, J. H. J., et al. 2016, *A&A*, **595**, A1  
 Gil, J., Haberl, F., Melikidze, G., et al. 2008, *ApJ*, **686**, 497  
 Gold, T. 1969, *Natur*, **221**, 25  
 Halpern, J. P., & Holt, S. S. 1992, *Natur*, **357**, 222  
 Harding, A. K. 2013, *FrPhy*, **8**, 679  
 Harding, A. K., & Muslimov, A. G. 2001, *ApJ*, **556**, 987  
 Harding, A. K., & Muslimov, A. G. 2002, *ApJ*, **568**, 862  
 He, C., Ng, C.-Y., & Kaspi, V. M. 2013, *ApJ*, **768**, 64  
 Hermsen, W., Kuiper, L., Hessels, J. W. T., et al. 2017, *MNRAS*, **466**, 1688  
 Hewish, A., Bell, S. J., Pilkington, J. D. H., Scott, P. F., & Collins, R. A. 1968, *Natur*, **217**, 709  
 Ho, W. C. G. 2011, *MNRAS*, **414**, 2567  
 Igoshev, A. P., Elfriz, J. G., & Popov, S. B. 2016, *MNRAS*, **462**, 3689  
 Jordi, C., Gebran, M., Carrasco, J. M., et al. 2010, *A&A*, **523**, A48  
 Kargaltsev, O., Durant, M., Misanovic, Z., & Pavlov, G. G. 2012, *Sci*, **337**, 946  
 Kargaltsev, O., Pavlov, G. G., & Garmire, G. P. 2006, *ApJ*, **636**, 406  
 Kramer, M., Bell, J. F., Manchester, R. N., et al. 2003, *MNRAS*, **342**, 1299  
 Liddle, A. R. 2007, *MNRAS*, **377**, L74  
 Lyne, A. G., & Lorimer, D. R. 1994, *Natur*, **369**, 127  
 Manchester, R. N., Hobbs, G. B., Teoh, A., & Hobbs, M. 2005, *AJ*, **129**, 1993  
 Mel'Nik, A. M., & Dambis, A. K. 2009, *MNRAS*, **400**, 518  
 Mereghetti, S., Kuiper, L., Tiengo, A., et al. 2016, *ApJ*, **831**, 21  
 Mewe, R., Gronenschild, E. H. B. M., & van den Oord, G. H. J. 1985, *A&AS*, **62**, 197  
 Misanovic, Z., Pavlov, G. G., & Garmire, G. P. 2008, *ApJ*, **685**, 1129  
 Oegelman, H., Finley, J. P., & Zimmerman, H. U. 1993, *Natur*, **361**, 136  
 Özel, F., & Freire, P. 2016, *ARA&A*, **54**, 401  
 Page, D., Lattimer, J. M., Prakash, M., & Steiner, A. W. 2004, *ApJS*, **155**, 623  
 Philippov, A., Tchekhovskoy, A., & Li, J. G. 2014, *MNRAS*, **441**, 1879  
 Popov, S. B., & Turolla, R. 2012, *Ap&SS*, **341**, 457  
 Posselt, B., Arumugasamy, P., Pavlov, G. G., et al. 2012a, *ApJ*, **761**, 117  
 Posselt, B., Pavlov, G. G., Manchester, R. N., Kargaltsev, O., & Garmire, G. P. 2012b, *ApJ*, **749**, 146  
 Possenti, A., Cerutti, R., Colpi, M., & Mereghetti, S. 2002, *A&A*, **387**, 993  
 Rigoselli, M., & Mereghetti, S. 2018, *A&A*, **615**, A73  
 Rosen, S. R., Webb, N. A., Watson, M. G., et al. 2016, *A&A*, **590**, A1  
 Ruderman, M. A., & Sutherland, P. G. 1975, *ApJ*, **196**, 51  
 Smith, R. K., Brickhouse, N. S., Liedahl, D. A., & Raymond, J. C. 2001, *ApJL*, **556**, L91  
 Strüder, L., Briel, U., Dennerl, K., et al. 2001, *A&A*, **365**, L18  
 Tsygankov, S. S., Wijnands, R., Lutovinov, A. A., Degenaar, N., & Poutanen, J. 2017, *MNRAS*, **470**, 126  
 Turner, M. J. L., Abbey, A., Arnaud, M., et al. 2001, *A&A*, **365**, L27  
 Verbunt, F., Igoshev, A., & Cator, E. 2017, *A&A*, **608**, A57  
 Viganò, D., & Pons, J. A. 2012, *MNRAS*, **425**, 2487  
 Wachter, K., Leach, R., & Kellogg, E. 1979, *ApJ*, **230**, 274  
 Wilms, J., Allen, A., & McCray, R. 2000, *ApJ*, **542**, 914  
 Yakovlev, D. G., & Pethick, C. J. 2004, *ARA&A*, **42**, 169  
 Yao, J. M., Manchester, R. N., & Wang, N. 2017, *ApJ*, **835**, 29  
 Zavlin, V. E., & Pavlov, G. G. 2004, *ApJ*, **616**, 452  
 Zavlin, V. E., Pavlov, G. G., & Shibano, Y. A. 1996, *A&A*, **315**, 141  
 Zhang, B., Harding, A. K., & Muslimov, A. G. 2000, *ApJL*, **531**, L135